

A Multi-Scale Model for Simulating Liquid-Hair Interactions

YUN (RAYMOND) FEI and HENRIQUE TELES MAIA, Columbia University CHRISTOPHER BATTY, University of Waterloo CHANGXI ZHENG and EITAN GRINSPUN, Columbia University





Fig. 1. Hair is submerged in water and then rapidly flipped, resulting in wet locks and dripping.

The diverse interactions between hair and liquid are complex and span multiple length scales, yet are central to the appearance of humans and animals in many situations. We therefore propose a novel multi-component simulation framework that treats many of the key physical mechanisms governing the dynamics of wet hair. The foundations of our approach are a discrete rod model for hair and a particle-in-cell model for fluids. To treat the thin layer of liquid that clings to the hair, we augment each hair strand with a height field representation. Our contribution is to develop the necessary physical and numerical models to evolve this new system and the interactions among its components. We develop a new reduced-dimensional liquid model to solve the motion of the liquid along the length of each hair, while accounting for its moving reference frame and influence on the hair dynamics. We derive a faithful model for surface tension-induced cohesion effects between adjacent hairs, based on the geometry of the liquid bridges that connect them. We adopt an empirically-validated drag model to treat the effects of coarse-scale interactions between hair and surrounding fluid, and propose new volume-conserving dripping and absorption strategies to transfer liquid between the reduced and particle-in-cell liquid representations. The synthesis of these techniques yields an effective wet hair simulator, which we use

This work is supported by the National Science Foundation, under grant Nos. 1409286, 1319483, and CAREER-1453101, Graduate Student Research Fellowship No. DGE-16-44869, the Natural Sciences and Engineering Research Council of Canada under grant No. RGPIN-04360-2014, the National GEM Consortium, Pixar, and Adobe.

Permission to make digital or hard copies of all or part of this work for personal or classroom use is granted without fee provided that copies are not made or distributed for profit or commercial advantage and that copies bear this notice and the full citation on the first page. Copyrights for components of this work owned by others than the author(s) must be honored. Abstracting with credit is permitted. To copy otherwise, or republish, to post on servers or to redistribute to lists, requires prior specific permission and/or a fee. Request permissions from permissions@acm.org.

@ 2017 Copyright held by the owner/author(s). Publication rights licensed to Association for Computing Machinery.

0730-0301/2017/7-ART56 \$15.00 https://doi.org/10.1145/3072959.3073630 to animate hair flipping, an animal shaking itself dry, a spinning car wash roller brush dunked in liquid, and intricate hair coalescence effects, among several additional scenarios.

CCS Concepts: • Computing methodologies → Physical simulation;

Additional Key Words and Phrases: wet hair, fluid dynamics, two-way coupling, shallow water equation, particle-in-cell

ACM Reference format:

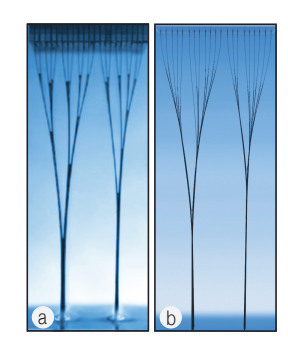
Yun (Raymond) Fei, Henrique Teles Maia, Christopher Batty, Changxi Zheng, and Eitan Grinspun. 2017. A Multi-Scale Model for Simulating Liquid-Hair Interactions. *ACM Trans. Graph.* 36, 4, Article 56 (July 2017), 17 pages. https://doi.org/10.1145/3072959.3073630

1 INTRODUCTION

Hair dynamics have long been a focus of computer animation because of their critical role in the appearance of humans and animals. Likewise, the pervasiveness of fluid phenomena in the physical world has led to extensive research into the simulation of gases and liquids. However, methods to capture the array of complex interactions between these ubiquitous phenomena have received less attention in the literature, and no model compatible with standard grid-based fluid solvers has been proposed.

The interaction between hair and liquid is inherently a multiphysics phenomenon that spans multiple spatial scales. When fully submerged in a body of liquid, underwater hair strands collectively behave as a kind of porous medium and introduce a drag effect on the surrounding flow. When removed from the liquid, hair inevitably retains a certain amount of liquid on its surface, which then flows along the hair strands and eventually drips off. Meanwhile,

Fig. 2. **Recursive structures** in wet hair coalescence. (a) A picture of physical laboratory experiment of Bico et al. [2004]. (b) Our simulated result with a similar setup.



wet hairs also interact with each other, not only through hair-hair collisions but also through surface tension effects of *liquid bridges* that connect wet hairs in close proximity—the latter denoting the physics that causes wet hair to cohere and coalesce into clumps.

Examination of the consequences of these multi-scale physics is critical to the design of an appropriate model. One exceptionally small length scale—the hair thickness—contrasts with a much larger length scale, the hair length. The very thin layer of liquid flow immediately surrounding the hair strand contrasts with bulk volumes of liquid with which the hair may also interact. Finally, the drag forces that affect fully submerged hairs differ dramatically from the out-of-liquid surface tension forces that arrange hairs into intriguing structures (Figure 2). A standard grid-based fluid simulator simply cannot efficiently resolve the thin surface liquid flowing over the hair, nor capture the detailed interactions between hair and liquid.

With these facts in mind, we propose a new framework to simulate a variety of hair-liquid interaction effects. We begin with two standard models for hair and liquid: a particle-in-cell Navier-Stokes liquid simulator [Jiang et al. 2015] and a Kirchhoff rod-based hair simulator [Bergou et al. 2010]. The observations above motivate our addition of a *second* fluid model to represent and track liquid directly *on the hair* itself. Specifically, we introduce a height-field representation for the smaller volume of liquid along and around each individual hair strand. Given this set of three physical representations for hair and fluid, we can enumerate and design a set of simulated physical interactions between them that are needed to faithfully reproduce wet hair effects. We have pursued precisely this program, yielding a framework with the following novel components:

- A reduced liquid model for flow along individual hair strands, which reduces by one dimension the shallow-water equations by invoking rotational symmetry and introduces inertial forces due to acceleration of the hair centerline;
- A model for surface tension-induced cohesion forces between wet hairs;
- A drag model for the forces between submerged hairs and a surrounding fluid volume;
- A model for dripping of reduced liquid off the hair;
- A model for capturing volumetric liquid onto the hair.

We will demonstrate that, collectively, these features enable a higher fidelity simulation of the compelling dynamics of wet hair than achieved by existing techniques.

2 RELATED WORK

Hair simulation. A survey of earlier hair simulation work can be found in the reviews by Ward et al. [2007] and Hadap et al. [2007]. More recently, several works have aimed towards making hair inextensible [Han and Harada 2013; Müller et al. 2012], or combining position based dynamics [Kugelstadt and Schömer 2016] with the discrete elastic rods (DER) framework [Bergou et al. 2010, 2008; Kaufman et al. 2014]. Additionally, Iben et al. [2013] proposed an artistic way to control curly hairs. As for collision between hairs, Kaufman et al. [2014] combined a nonlinear integrator with a Gauss-Seidel collision solver, while Gornowicz and Borac [2015] proposed a hybrid algorithm for higher performance and better stability. To simulate the underlying dynamics of hair, we adopt the DER framework, and model both the cohesive and repulsive effects as constraints. We solve them with a stable constraint solver [Tournier et al. 2015] alongside a modified conjugate gradient preconditioner. We choose such an implementation for simplicity, although we believe more sophisticated integrators or constraint solvers [Gornowicz and Borac 2015; Kaufman et al. 2014] could also be applied for the constraints proposed in this paper.

Fluid simulation. Our model for bulk fluid volumes relies on an affine particle-in-cell (APIC) simulator [Jiang et al. 2015]; Bridson [2015] provides a thorough review of grid-based methods for fluid simulation more broadly. Recent techniques for animating fluid-hair interactions have instead built on the smoothed particle hydrodynamics (SPH) family of methods [Ihmsen et al. 2014; Monaghan 1994; Müller et al. 2003]. We adopt APIC for convenience, but it is likely also possible to port our model to other numerical formulations of fluid dynamics.

Wet hair in animation. Early explorations of wet hair focused on modifying the physical properties of a basic hair model, such as mass or material stiffness, to approximate the effects of wetting, styling, or drying [Bertails et al. 2005; Ward et al. 2004].

Rungjiratananon et al. [2012] proposed two-way interactions between SPH-based water and a shape-matching hair model using a porous flow approach for the propagation of liquid inside the hair. They discretized the porous flow model on a regular Cartesian grid in a bounding box surrounding the hair, adapting earlier SPH-based porous flow techniques [Lenaerts et al. 2008]. Spring-like sticking forces between adjacent hairs were used to approximate wet hair cohesion, and the change in the hair's rest-shape was dictated by the user. While absorption and dripping are handled through porous flow, full two-way coupling, in the sense of the hair and bulk fluid applying mutual forces, is neglected. Lin et al. [2014; 2015] proposed a similar porous flow model, but further incorporated two-way fluid-hair interactions, using SPH for the fluid and the DER model for hair. They also disabled hair-hair adhesion forces for underwater hairs to better handle fully submerged regions.

A few authors have treated hair itself as a fluid-like material, either to approximate internal forces [Hadap and Magnenat-Thalmann 2001] or to accelerate collision processing [McAdams et al. 2009].

Brute force fluid-structure interaction. When sufficient computational power is available, fine-scale simulations of interaction









Fig. 3. Water flowing over and through a sloped mat of fur, causing initially straight hair to clump and become flattened by the weight of water captured by the strands.

between structures (such as hair) and grid-based fluids can be performed, often using embedded or immersed boundary methods [Mittal and Iaccarino 2005]; conceptually analogous solid-fluid coupling schemes have been applied to animation problems involving rigid bodies, deformables, or cloth (e.g., [Batty et al. 2007; Robinson-Mosher et al. 2008]). However, to properly handle hair, the fluid would have to be simulated on a grid that is sufficiently fine that each hair diameter spans at least a few cells. While such brute-force methods have the potential to be extremely accurate, and potentially useful for deriving coarse-scale models, this strategy is far too costly to be directly applied to scenarios with hundreds or thousands of

Porosity and drag effects. In aggregate, a large collection of hair fibers submerged in fluid acts as a semi-permeable barrier which fluid can flow through only slowly [Jackson and James 1986]. This leads to an assumption of a body of hair as a porous medium, which has also been adopted by the previous hair-fluid coupling models in graphics. Stylianopoulos et al. [2008] performed direct simulations of fluid flowing through submerged fiber assemblies in order to derive an empirical coarse-scale drag/permeability model depending on fiber volume fraction, radius, and orientation. We adopt this drag model in our work. Simpler interaction models have also been used in computer animation, such as an external force computed from a procedural wind-field or a non-coupled fluid simulation (e.g., [Selle et al. 2008]).

Capillary bridges and coalescence. At small scales, the surface tension of liquid layers on hair or sediment particles in close proximity often lead to what are called liquid bridges or capillary bridges [Meseguer and Sanz 1985]. That is, a continuous body of liquid joins the two solids together, often taking on a minimal surface-like shape. A liquid bridge induces attractive forces between the solids that it joins together because surface tension acts to minimize the total exposed liquid surface area. This effect is responsible for the cohesion of wet hair, leading to the familiar effect of hair clumping (or fiber coalescence) [Bico et al. 2004; Duprat et al. 2012; Py et al. 2007; Singh et al. 2014]. Brute-force volumetric simulation has been used to study the behavior of liquid bridges and the resulting forces [Virozub et al. 2009]. The cohesive behavior of liquid bridges is an instance of a broader set of phenomena driven by elastocapillarity, or the interplay between surface tension in liquids and elasticity in solids [Roman and Bico 2010].

Surface flows. We distinguish two dominant directions in which water in contact with hair may flow: along the axis of a single hair strand, and between hairs, i.e., transport from one strand to the next. Indeed, according to Q. Wang et al. [2014] who studied the behavior of paint brushes, liquid flows mostly on the hair surface or between hairs, rather than *inside* the hair itself. The experimental studies of Barba et al. [2013] likewise indicate that flow inside hair cuticles is very slow (on the order of hours) and contributes only to secondary effects. While interpreting hair as a porous material is a reasonable approximation, inertial effects must still be considered for porous media at moderate to large Reynolds numbers, as discussed by Hellström and Lundström [2006]. This is certainly the case for the wet hair flipping or spinning car wash brushes we consider, for example. We therefore choose to treat flow along individual hair strands with a shallow water model that includes inertia, and the flow among hairs as a slower capillary flow process [Washburn 1921]. Our shallow water model is adapted from the work of H. Wang et al. [2007], who considered generalized shallow water on triangle mesh surfaces rather than rods.

Our choice contrasts with previous work on animating wet hair [Lin 2014, 2015; Rungjiratananon et al. 2012], which assumes that liquid flows in the Darcy regime (i.e., porous flow without inertia or convection) inside the entire hair region, including the hair cuticles and the space between hairs.

Another alternative assumption in the literature is that of thin film or coating flow, which is similar to the Darcy regime, but with convection considered. In this case, the Navier-Stokes equations can be reduced to a fourth-order PDE in which viscosity dominates and inertia is negligible [Craster and Matar 2006]. This model has recently been used in graphics to animate thin films flowing on triangle meshes [Azencot et al. 2015]; while our physical model differs, we adapt elements of their discretization technique.

Splashing. Thoroughly wet hair being whipped at high speeds gives rise to dramatic splashing effects, as can be seen in the flipping of wet hair or the shaking behaviors of wet dogs drying themselves; yet there has been relatively little study of these effects. The exception is the work of Dickerson et al. [2012], who showed that mammals tend to shake at carefully chosen frequencies that depend on body mass and the properties of water.

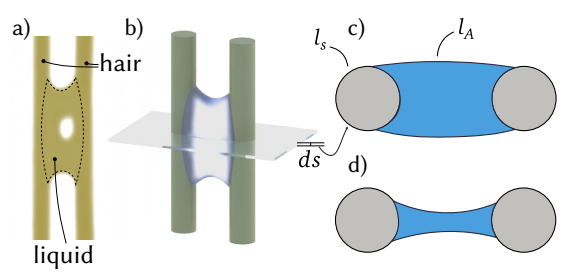


Fig. 4. A liquid bridge. (a) Labeled microscopic photo of liquid held by hairs, courtesy of Wang et al. [2014]; (b) rendered figure of the geometry; (c) cross section of a slice of the geometry; (d) another possible cross section with less liquid.

3 WET HAIR PHYSICS

We begin by describing our physical models in the continuous setting, which are specifically tailored to capture hair-liquid dynamics at different scales and in different configurations. We derive a new surface tension model to compute forces between hairs that are bridged by liquid (§3.1); we derive a dimensionally-reduced model of liquid flow on the hair surface, in a manner analogous to shallow water flow, to simulate liquid flows along and between hair strands (§3.2); and we introduce a drag force model to account for the interactions between submerged hairs and the surrounding liquid (§3.3). A list of notations used below is provided in our supplemental material (§S6).

3.1 Force between Hairs

We derive a new force model that computes the surface tension force between two wet hairs in proximity. This force tends to pull the hairs together, but is balanced by collision forces when two hairs contact each other. We also extend our surface tension model to compute adhesive forces between wet hairs and objects.

3.1.1 Cohesion due to Surface Tension. When two wet hairs are in proximity, a liquid bridge is formed (Figure 4). Microscopically, liquid molecules attract each other due to their cohesive forces, which creates a pressure imbalance at the surface causing the liquid to contract towards a minimal area configuration, subject to conservation of volume. Our surface tension model uses a formulation based on the surface potential energy, the energy needed to form liquid surface area. The surface tension force is the differential of this surface potential.

Consider a 2D cross section of two hairs connected by a small drop of liquid, as depicted in Figure 4. With the notation introduced therein, the surface potential over an infinitesimal volume near the cross section is proportional to its surface area, expressed as

$$dE_s = \sigma \left[l_A(s) + \cos \theta l_S(s) \right] ds, \tag{1}$$

where σ is the surface tension coefficient of the liquid-air interface (i.e., 71.97dyn/cm for water at a room temperature of 298.15K). The equilibrium contact angle, θ , at which the liquid-air interface meets the liquid-hair interface is a constant that depends on the material properties of liquid, air, and hair. The arc lengths of the liquid-air and hair-air boundary are given by $l_{\rm A}$ and $l_{\rm S}$, respectively (Figure 4-c), and ds is an infinitesimal length along the centerline of the hairs. Since ${\rm d}E_{\rm S}$ can vary along the hair's centerline, the total surface

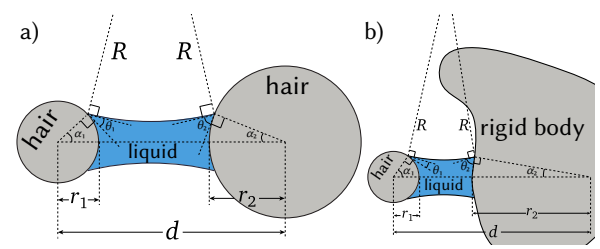


Fig. 5. Notation for a liquid bridge cross section.

potential is an integral over the length $\Omega_{\rm L}$ of the hairs (i.e., $\int_{\Omega_{\rm L}} {\rm d}E_s$). The expression (1) can be derived using Young's equation [Young 1805]; details are given in Section S1 of our supplemental document.

Our cohesion model builds on the investigation of Liu et al. [2007]. We summarize their argument and then indicate our point of departure. First, when two hairs are close, surface tension dominates over gravity. If we ignore gravity, we notice that the top and bottom liquid-air interfaces must be symmetric, consisting of two circular arcs. This is because the surface energy contributed by molecular cohesive forces is uniformly distributed over the interfaces. Following the notation in Figure 5, the cross-sectional surface potential is expressed as

$$dE_s = \sigma \left[l_A(s) + \cos \theta_1 l_{S1}(s) + \cos \theta_2 l_{S2}(s) \right] ds, \tag{2}$$

where l_{S1} and l_{S2} are the arc lengths of the two hair-air boundaries, and θ_1 and θ_2 are the contact angles. (In this case, they are a known constant, $\theta_1 = \theta_2 = \theta$, as discussed earlier.) Let r_1 and r_2 be the radii of the two hairs, and R be the radius of the circle corresponding to the liquid surface arcs. Since the liquid is bounded by circular arcs, the length of the liquid-air interface is given simply by

$$l_{A}(s) = R \left[\pi - (\theta_{1} + \alpha_{1} + \theta_{2} + \alpha_{2}) \right]$$
 (3)

and the length of the hair-air interface by

$$l_{Si}(s) = 2r_i(\pi - \alpha_i), \quad i = 1, 2.$$
 (4)

However, what we would ultimately like to know is the dependence of the energy on the distance d between hairs. Therefore, we next need to find the dependence on d of R and α_i above.

Geometric arguments can be used to show that the distance d can be expressed as

$$d = R \sum_{i=1,2} \cos(\theta_i + \alpha_i) - \sum_{i=1,2} r_i (1 - \cos \alpha_i), \tag{5}$$

and the cross-sectional area of the liquid region, A_L , as

$$A_{L} = -\pi R^{2} + \sum_{i=1,2} \left[\frac{1}{2} r_{i}^{2} \sin 2\alpha_{i} + 2r_{i}R \sin \alpha_{i} \cos(\theta_{i} + \alpha_{i}) \right] +$$

$$\sum_{i=1,2} \left[R^{2} \left(\theta_{i} + \alpha_{i} + \frac{1}{2} \sin(2\theta_{i} + 2\alpha_{i}) \right) - \alpha_{i} r_{i}^{2} \right].$$

$$(6)$$

Liu et al. [2007] apply a variation of these equations to an analysis of capillary rise between cylinders, subject to fixed boundary conditions (hair positions).

In a point of departure, we assume that the hair positions are variable, and employ these equations to determine the dependence of the surface energy on the distance d between hair centerlines, thereby yielding the inter-hair surface tension forces as the gradient of this energy.



Fig. 6. Two wet hairs held close and then pulled apart. Left: Hair strands freely separate without cohesion. Right: Cohesion forces cause hair strands to adhere. Note: for better visibility of small-scale illustrative examples in paper images (only), the radius of hair and reduced-liquid have both been scaled up.

Liu et al. [2007] also showed that the arc lengths of the solid-liquid interfaces are equal, i.e., $r_1\alpha_1=r_2\alpha_2$. Substituting this relationship into (5) and (6) above and differentiating both sides yields (dropping the subscript on α and using $\alpha\equiv\alpha_1$ for brevity)

$$\begin{bmatrix} \frac{\partial A_L}{\partial R} & \frac{\partial A_L}{\partial \alpha} \\ \frac{\partial d}{\partial R} & \frac{\partial d}{\partial \alpha} \end{bmatrix} \begin{bmatrix} \frac{\partial R}{\partial d} \\ \frac{\partial \alpha}{\partial d} \end{bmatrix} = \begin{bmatrix} \frac{dA_L}{dd} \\ \frac{d}{dd} \end{bmatrix} = \begin{bmatrix} 0 \\ 1 \end{bmatrix}, \tag{7}$$

where $\frac{dA_L}{dd}$ vanishes in the second equivalence. Since the longitudinal dimension is much larger than the transverse dimensions for hairs, we approximate the area of the liquid region to be constant as d changes. In turn, the fluid incompressibility is respectively enforced in the longitudinal and transverse dimensions. The left-hand-side Jacobian matrix can be analytically computed from (5) and (6). We then solve this 2×2 system for $\frac{\partial R}{\partial d}$ and $\frac{\partial \alpha}{\partial d}$. At last, we can evaluate the cross-sectional surface tension force using

$$f_s = \frac{\mathrm{d}}{\mathrm{d}d} \mathrm{d}E_s = \frac{\partial \mathrm{d}E_s}{\partial R} \frac{\partial R}{\partial d} + \frac{\partial \mathrm{d}E_s}{\partial \alpha} \frac{\partial \alpha}{\partial d}, \tag{8}$$

where both derivatives $\frac{\partial \mathrm{d}E_s}{\partial R}$ and $\frac{\partial \mathrm{d}E_s}{\partial \alpha}$ will be computed by plugging (3) and (4) into (2) and differentiating analytically. Details of the method of evaluating f_s are deferred to §4.1.1.

As depicted in Figure 2, our liquid-bridge based model of cohesion is able to reproduce the tree structures observed in the laboratory experiments of Bico et al. [2004].

Adhesive forces between hairs and solids. We can straightforwardly extend our surface tension model to determine the adhesive force between a hair and a solid object resulting from liquid bridges. The local geometry of a solid object can be approximated by a sphere whose curvature agrees with the local mean curvature of the solid object (Figure 5b). This approximation allows us to apply the surface tension model developed above, with two modifications: 1) using different contact angles to account for the solid object's material being different from the hair, and 2) using the radius of the local sphere that approximates the solid during the computation of the hair-body force (i.e., the reciprocal of the body's local curvature replaces r in the equations above).

3.1.2 Collision Forces. We adopt a simple penalty model to treat collisions and contact. Consider two hairs, each with radius r, having a distance d between their centerlines. Both surface tension and contact forces between the hairs depend solely on the distance d, but each dominates at a different d: penalty forces dominate when hairs overlap one another (d < 2r, where r is the hair radius), while surface tension dominates when hairs are separated but at a distance smaller than d_{\max} , a critical value at which the liquid bridge between the hairs breaks. Physical experiments have shown that d_{\max} depends on the equilibrium contact angle θ and the

cross-sectional liquid area A_L (defined in (6)) through an empirical relationship [Lian et al. 1993],

$$d_{\text{max}} = (1 + 0.5\theta)\sqrt{A_L}.\tag{9}$$

At some distance d_0 between 2r and d_{max} , the penalty force balances surface tension, and the net force vanishes.

Surface tension and collision penalty forces by nature conflict with each other. Later, in our numerical simulation, if we compute them separately in each simulation step, we need either many iterations or tiny timesteps until both forces reach a balance. To avoid this difficulty, we reconcile them in a single force model described as a piecewise function,

$$f(d) = \begin{cases} k(d - d_0), & \text{if } d < 2r, \\ \frac{d - d_0}{B - d_0} \tilde{f}_S(d), & \text{if } 2r \le d < d_0, \\ \frac{d - d_0}{B - d_0} f_S(B), & \text{if } d_0 \le d < B, \\ f_S(d), & \text{if } B \le d < d_{\text{max}}. \end{cases}$$
(10)

Here k is the stiffness of the penalty force. The distance value B is chosen to allow a smooth (linear) transition from $f(d_0)=0$ to the surface tension force $f(B)=f_s(B)$. In practice, we use $B=2d_0-2r$. The function $\tilde{f}_s(d)$ interpolates values between f(2r) and $f(d_0)=0$, expressed as

$$\tilde{f}_s(d) = \frac{(d - d_{\min})f_s(B) + k[(d + B - d_0)d_0 - dB]}{d_0 - d_{\min}}.$$
 (11)

Figure 7 plots a typical force profile with respect to d. We use $d_0 = 3r$ throughout our implementation. Note that in (9), if the hair is dry, $A_L = 0$ and thus $d_{\text{max}} = 0$; we therefore simply ignore the two formulas in the bottom of (10) and thus naturally handle the case of dry hair.

This combined model for contact and hair adhesion forces is straightforward to implement, reasonably efficient, and avoids the stability issues that arise for staggered/decoupled treatments.

3.2 Liquid Flow over the Hair Surface

Flow along hair. Wet hairs are covered by a thin layer of liquid flowing on the hair surface. Simulating the surface flows using the standard Eulerian approach is intractable, because the thin liquid layer and the long hair length relative to the tiny hair radius would demand an excessively fine Eulerian grid. However, we can exploit this disparity in length scales to approximate the liquid flow using a dimension-reduced model as in the shallow liquid equations [Kass

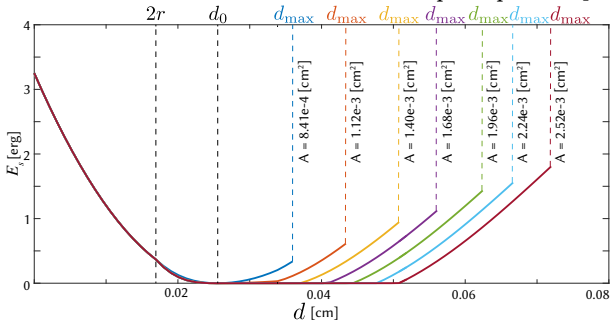


Fig. 7. Plot of the potential energy of the combined cohesion/repulsion force vs. distance between two hairs with unit length. Curves are cut off at d_{max} .

and Miller 1990; Vreugdenhil 1994; Wang et al. 2007]. In this way, the liquid's motion can be described in the reference frame of the hair; however, we must also consider the effects of the motion of this non-inertial reference frame itself. Thus the reduced liquid's velocity has two components: the *intrinsic* hair-reduced liquid velocity, i.e., velocity of shallow liquid-like flow with respect to the hair; and the *extrinsic* hair-reduced liquid velocity, i.e., the velocity of the liquid due to the motion of the hair that carries it.

Additionally, because of the small hair radius, the transversal liquid flow *around* a hair strand occurs on a much smaller time scale in comparison to longitudinal flows. Thus, we assume a quasi-static liquid layer thickness that distributes uniformly at a transversal cross section of the hair, while the thickness along the hair can vary. We apply this approximation to all hairs, even in the presence of close contact between different hairs.



This choice allow us to derive a 1D reduced-dimensional model in a manner analogous to the shallow water equations (see Section S2 of our supplemental document for the derivation details), and strikes a balance between strict physical validity and practical computational expense. We model the 1D longitudinal intrinsic reduced velocity \boldsymbol{u} and liquid layer radius \boldsymbol{h} with the governing equations

$$\frac{\partial u}{\partial t} = -u \frac{\partial u}{\partial x} - \frac{1}{\rho_L} \frac{\partial p}{\partial x} + a, \tag{12}$$

$$\frac{\partial (h+r)^2}{\partial t} + \frac{\partial}{\partial x} \left[\left((h+r)^2 - r^2 \right) u \right] = 0, \tag{13}$$

where u, h, and p are all 1D functions along the hair, parameterized by the coordinate x. The variable p is the hydrostatic pressure value over a cross section, ρ_L is the liquid density, a is the acceleration introduced by external forces (such as gravity and inertial forces), r is the hair radius, and h is the liquid layer thickness. Physically, (12) is derived from conservation of momentum; (13) is derived from conservation of mass, and describes the advection of liquid as the temporal evolution of layer thickness h. We defer the computation of the inertial force (Figure 8) to the discrete setting, in §4.2.

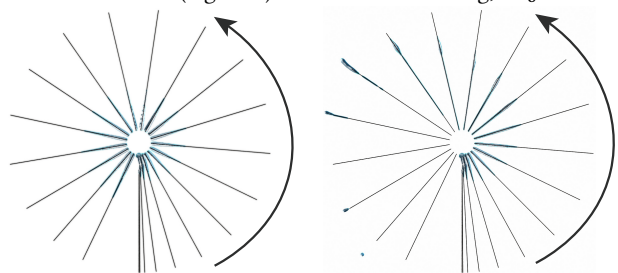


Fig. 8. Inertial force: When a hair rotates about a central point, centrifugal forces cause the liquid to flow towards and off the tip. We compare our simulation without (left) and with (right) the inertial force. Time-slices are shown in order proceeding counter-clockwise from the bottom.

Momentum transport along hair. The thin layer of liquid weighs down the hair by an additional mass density of $\pi(h^2 + 2hr)$. Consequently, the evolution of h—transport of liquid along the hair—alters the effective mass distribution of the hair. This is critical to consider because the Lagrangian hair is itself a dynamic system; redistributions of mass along the hair, without redistributions of velocity,

would lead to sudden changes in the hair momentum, and corresponding artifacts in motion.

To properly account for evolution of the hair state due to reduced-liquid, we therefore transport hair *momentum* according to the same reduced-liquid equations. After updating the (intrinsic) reduced-liquid velocity with (12) and the height field with (13), we also solve four additional transport equations,

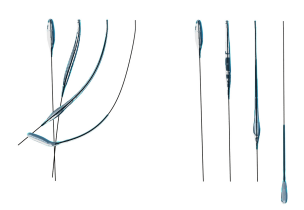
$$\frac{\partial}{\partial t} \left[\boldsymbol{v}_{H_i} \left((h+r)^2 - r^2 \right) \right] + \frac{\partial}{\partial x} \left[\boldsymbol{v}_{H_i} \left((h+r)^2 - r^2 \right) \boldsymbol{u} \right] = 0, \quad (14)$$

$$\frac{\partial}{\partial t} \left[\omega \left((h+r)^4 - r^4 \right) \right] + \frac{\partial}{\partial x} \left[\omega \left((h+r)^4 - r^4 \right) \boldsymbol{u} \right] = 0, \quad (15)$$

where $i \in \{x, y, z\}$ are the labels for three components of the Lagrangian hair velocity, \boldsymbol{v}_{H_i} , and ω is the angular velocity in the degree of freedom for hair twisting.

This physically principled approach is more costly than evolving mass alone, but it avoids the artifacts of ignoring momentum conservation. For example, a naïve alternative might be to *locally* preserve momentum by rescaling the local hair velocity based on its updated mass; however, this ignores the momentum of the liquid flowing along the hair.

Fig. 9. A droplet sliding down a single vertical hair as it moves under uniform horizontal velocity. Under (only) downward gravitational acceleration, the hair should remain vertical, in the absence of external horizontal forces. We compare naïve local momentum rescaling (left) versus our momentum update transport (right).



In Figures 9 and 10, we show two scenarios of a droplet sliding on a single hair, illustrating that our method produces physically meaningful results, while naïve rescaling produces severe motion artifacts in the hair.

Fig. 10. A droplet sliding down a single hair, causing it to swing. Left: Naïve rescaling leads to severe spurious bending. Right: Our momentum transports gives a natural motion.

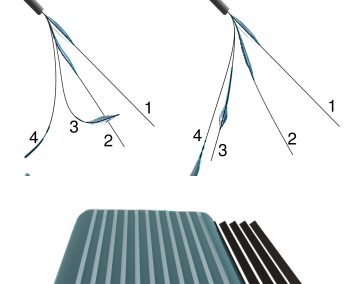




Fig. 11. Left: Reduced-liquid is assigned to several hairs at the left of a longer set. Right: Transversal capillary flow steadily propagates the liquid to adjacent hairs.

Flow across hairs. In addition to flowing along (and around) individual hair strands, liquid may also flow transversally across multiple hairs (Figure 11). This phenomenon can be seen in the spread of moisture between the hairs of a wet paint-brush or in the slow





Fig. 12. Reduced-liquid flow and dripping on a single strand. Left: No reduced-liquid flow. Center: Reduced-liquid flow without dripping; the liquid flows towards the tip and disappears. Right: Reduced-liquid with dripping enabled.



Fig. 13. A comparison of liquid flow on a coiled hair strand. Left-Top: Neither reduced-liquid flow nor dripping enabled. Left-Bottom: With reduced-liquid flow enabled the liquid accumulates in the center and the hair sags. Right: Enabling dripping lets the liquid flow off the hair.

impregnation of wood and other porous materials with liquids—generally known as *capillary flow* [Washburn 1921]. Capillary flow spreads in the transversal direction slowly and is driven mainly by pressure differences. Following the previous studies, the transversal flow velocity u_t is solely determined by the pressure gradient,

$$u_t = -\frac{r^2 + 4r}{8\mu} \nabla_t p,\tag{16}$$

where r is the radius of capillarity which we assume is approximately the hair radius, and μ is the fluid viscosity. We once incorporated the numerical computation of this flow into our discrete reduced-liquid model described in §4.2. However, ultimately we found that this transversal flow is not visually significant for the kinds of scenarios we have considered (with the exception of Figure 11). For this reason, our animation examples (see the supplemental video) are computed without transversal flow.

Dripping from hairs. For liquid on the tip of a hair, the amount dripping off is simply determined by the flux of velocity off the tip (or zero, if the velocity is directed away from the tip). However, since an individual hair also cannot support an arbitrary amount of liquid at any given point along its length, we must determine a threshold for the local liquid volume allowed, and a mechanism to treat the excess liquid that drips off at that point (see Figure 12 and Figure 13).

We use a threshold determined from theory of capturing droplets with thin fibers [Lorenceau et al. 2004]: given a region filled with N fibers, the averaged intensity of acceleration $a_{\hat{n}}$ applied on the normal directions of flows (perpendicular to the tangential direction of the hair), the surface tension coefficient σ , the radii of a thin fiber r, and the density of liquid ρ_L , the surface tension force applied is $4\pi r \sqrt{N}\sigma$. To capture the liquid we need the surface tension force to balance the other forces applied on the liquid, which is $\rho_L a_{\hat{n}} V$, where V is the volume of liquid attached to the small segments of hairs. Hence the maximal radius of droplet that can be held by the

hair segments is computed as

$$r_{\text{max}} = \left(\frac{3r\sigma\sqrt{N}}{\rho_L a_{\hat{n}}}\right)^{1/3}.$$
 (17)

N is computed by counting how many hairs intersect with a given grid voxel. After determining the maximum radius of liquid droplet that can be held by these N hairs, we remove the extra volume of liquid from the hairs and release them as APIC particles in accordance with Equ. 17, where any liquid outside the extent of $r_{\rm max}$ is free to drip away from the hairs.

3.3 Darcy-Forchheimer Drag Force for Submerged Hairs

When hairs are fully submerged in liquid, their motion is affected by the flow of the surrounding liquid, in addition to the inter-hair collision forces (but *not* surface tension forces). In the cases that we primarily focus on, hairs are often densely distributed. They interact with the liquid, collectively behaving like a porous media [Jackson and James 1986]. Therefore, we apply the classic Darcy's law (or Darcy-Forchheimer drag forces) to compute the interaction force between hairs and liquid.

Intuitively, the Darcy-Forchheimer drag force tends to reduce the velocity difference between hair strands and their surrounding liquid. Formally, consider a point \boldsymbol{x} of a submerged hair. The drag force induced by the liquid is modified from Whitaker [1996] as

$$\mathrm{d}f_{\mathrm{d}}(\mathbf{x}) = -\frac{1}{2} \left[\mu \mathsf{A}(\vartheta) \delta \mathbf{u}(\mathbf{x}) + \mathsf{B}(\vartheta) \| \delta \mathbf{u}(\mathbf{x}) \| \delta \mathbf{u}(\mathbf{x}) \right] \mathrm{d}S, \tag{18}$$

where μ is the fluid viscosity, $\delta u(x)$ is the difference between the surrounding fluid velocity $u_F(x)$ at x and the hair velocity $v_H(x)$ (i.e., $\delta u(x) = u_F(x) - v_H(x)$), and the force will be integrated on the longitudinal cross section of hair dS. The A and B parameters are, respectively, the linear and quadratic drag tensors that relate δu with the drag force. Both depend on the specific submerged structure through the angle ϑ between the hair direction and the direction of relative velocity $\delta u(x)/\|\delta u(x)\|$.

We adopt an empirical drag force model [Stylianopoulos et al. 2008] which emerged from a study of the permeability of oriented fiber networks. Experiments have shown that the longitudinal drag d_{\parallel} (along the hair direction) is different from the perpendicular drag d_{\perp} (normal to the hair direction). Prior studies have derived both drag forces [Drummond and Tahir 1984; Sangani and Acrivos 1982]:

$$d_{\parallel} = \frac{4\pi}{-\ln\phi - 1.476 + 2\phi - 0.5\phi^2} \text{ and}$$

$$d_{\perp} = \frac{8\pi}{-\ln\phi - 1.476 + 2\phi - 1.774\phi^2 + 4.078\phi^3}.$$
(19)

Here, ϕ is the volume fraction of hairs in a cylindrical neighborhood volume Ω_L centered at \boldsymbol{x} (see inset figure), namely,

$$\phi = \frac{1}{V_{\Omega_L}} \sum_j V_{\Omega_{H_j} \cap \Omega_L},$$



where V_{Ω_L} is the volume of Ω_L , and $\Omega_{H_j} \cap \Omega_L$ indicates the volume of a hair j that occupies part of Ω_L . With

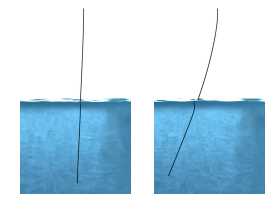
these quantities introduced, the drag tensor A is a similarity transformation of a diagonal matrix, specified by d_{\perp} , d_{\perp} , and d_{\parallel} :

$$\mathsf{A}(\vartheta) = \mathsf{R}^T(\vartheta) \begin{bmatrix} d_\perp & 0 \\ d_\perp \\ 0 & d_\parallel \end{bmatrix} \mathsf{R}(\vartheta),$$

where $R(\theta)$ is the rotation matrix that transforms a vector in the world frame of reference to the hair's local frame of reference at x. Lastly, B is related to A through [Ergun 1952; Nithiarasu et al. 1997]

$$\mathsf{B}(\vartheta) = \frac{1.75}{\sqrt{150}} \rho_L \mathsf{A}^{\frac{1}{2}}(\vartheta).$$

Fig. 14. A hair suspended by its tip moving left to right through liquid, with the drag force disabled (left) and enabled (right).



4 NUMERICAL SIMULATION

Having described our physical models, we now present the numerical methods we use to discretize and couple these models together, and thereby simulate hair-liquid interactions.

Method overview. The simulation consists of three interacting components: hair strands simulated using the discrete elastic rods (DER) method [Bergou et al. 2010, 2008]; bulk liquid simulated using the affine particle-in-cell (APIC) method [Jiang et al. 2015]; and hair-reduced liquid modeled using a novel formulation.

At the beginning of each time step, the hair, bulk- and reduced-liquid are advected separately. We then transfer the bulk- and reduced-liquid velocities onto a shared staggered background grid, which unifies the liquid momentum associated to the two representations, and serves to exchange momentum, drag and pressure forces in APIC style. Each grid face stores a (normal) velocity flux and density, sufficient to reconstruct the momentum flux across the face.

Figure 15 provides a visual overview of our algorithm and the flow of data through it for a single time step. The individual steps are:

- (1) Advect the APIC particles.
- (2) Solve the hair dynamics (§4.1), incorporating the drag force using velocities sampled from the grid (§3.3), adhesive/repulsive forces between hairs (§4.1.1), and the pressure impulse from the liquid stored from the previous step (§4.3).
- (3) Advect and apply forces to the reduced-liquid on the hair (§4.2).
- (4) Transfer the velocity of the APIC particles onto the grid (§4.3.1).
- (5) Apply the Lagrangian drag force from the hair onto the grid in an Eulerian style (§4.3.2).
- (6) Transfer the velocity of the reduced liquid onto the grid (§4.3.3).
- (7) Solve the Poisson equation and perform pressure projection (standard incompressible fluid solver).
- (8) Transfer the grid velocity back to the particles with APIC (§4.3.4).
- (9) Update the velocity of the reduced liquid due to surrounding pressure (§4.3.5).

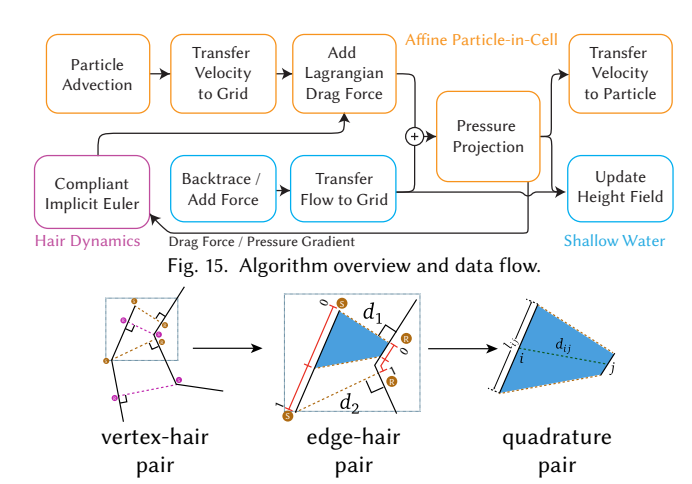


Fig. 16. We employ an adaptive quadrature to evaluate the cohesion forces. From left to right: potentially-connected vertex-hair pairs, connected edgehair pairs, and quadrature pairs.

(10) Exchange liquid volume between APIC and reduced-liquid domains through capture and dripping, accounting for conservation of mass (§4.4).

4.1 Hair Simulation

We discretize a hair as a sequence of vertex masses endowed with the viscoelastic stretching, bending, and twisting forces of the discrete elastic rod model based on Kirchhoff rod theory [Bergou et al. 2010, 2008].

4.1.1 Discretization of Cohesion and Contact Model. When wet, proximate hairs adhere due to a strong cohesive force (10). Because this force is strongly nonlinear in the inter-hair distance, and vanishes at distance $d_{\rm max}$, a naive evaluation strategy is prone to spatiotemporal discontinuities with attendant instabilities and "popping" artifacts.

To enforce spatiotemporal continuity of the force we employ the adaptive quadrature method depicted in Figure 16, which employs a single-point quadrature at the centroid of the *adapted subdomain* consisting of distances closer than $d_{\rm max}$; the crucial aspect is that the boundary (and therefore centroid) of the adapted subdomain varies smoothly with vertex positions, ensuring that the force is first-order continuous. To simplify the computation, we make the gross approximation that inter-hair closest-point distances vary linearly along an edge (in actuality, they are piecewise linear/quadratic). Therefore, our closest-point distances are only accurate at the vertices, but since the approximation still guarantees smoothly varying adapted subdomains, our central concern is heeded.

We build a graph between the hair segments in two phases, as depicted in Figure 16. In the following, recall that the cohesion cut-off distance $d_{\rm max}$ is a function (9) of the cross-sectional liquid area.

Phase 1: Identify potentially-connected vertex-hair pairs. For each hair (source) vertex, we consider all other hairs as candidate receivers. If the closest point on a candidate receiver is within distance $\frac{3}{2}d_{\max}(A_{\max})$, we say that the source vertex is potentially connected

to the *receiving hair*. To be conservative in finding all potential pairs, we assume the maximum area A_{max} that can be stored at the vertex, from (17). For each source vertex, we thus accumulate all those receivers that are proximate. This phase is accelerated by broad-phase culling that accounts for the threshold $\frac{3}{2}d_{\max}(A_{\max})$.

Phase 2: Identify connected edge-hair pairs. For each vertex-hair pair, we independently examine the (one or two) edges incident on the source vertex to determine if this source edge is connected to the receiving hair.

Consider one such source edge. By definition, at least one of its endpoints is a source vertex. We compute a threshold distance d_{max} using the sum of the liquid areas at the source vertex and receiving point. If the source-receiver distance computed in Phase 1 is below d_{max} , the source vertex is a *subdomain delimiter*. We likewise determine if the other endpoint is a delimiter.

If neither edge endpoint is a subdomain delimiter, we discard the edge; otherwise, we have identified a source edge that is connected to a receiving hair.

To establish a quadrature rule for this connected edge-hair pair, we first identify the quadrature subdomain on the source edge: if both edge endpoints are delimiters, the subdomain covers the entire edge, or barycentric interval [0, 1]; if one source vertex is a delimiter, it remains to find the other boundary of the subdomain. Suppose that the first vertex is a delimiter with distance $d_1 < d_{\max_1}$ and the second vertex is a non-delimiter with distance $d_2 > d_{\max_2}$. We set the barycentric coordinate of the second boundary at d = $d_{\rm max}$ by linearly interpolating from the edge endpoints via $\alpha =$ $(d_{\max_1} - d_1)/(d_{\max_1} - d_1 - d_{\max_2} + d_2)$, yielding the subdomain with barycentric interval $[0, \alpha]$.

While the quadrature subdomain on the source edge covers at most one edge, the corresponding receiving subdomain in general covers some contiguous region of the centerline, not contained within an edge. To identify this region, we first map each source edge endpoint to its receiving endpoint, which lies on the centerline but generally not at a vertex. Treating the two receiving endpoints as the delimiters of the real interval [0, 1], we map the barycentric interval $[0, \alpha]$ into corresponding positions on the receiving centerline.

Once the source and receiving subdomains are identified, their corresponding midpoints are chosen as the evaluation points for our single-point quadrature method.

Force computation. The quadrature subdomain established above allows us to discretize the cohesion force (2). Given a matched pair of subdomain midpoints indexed i and j, the adhesive force is computed as

$$f_{s,ij} = -w_{\text{FF}} \frac{\partial dE_{s,ij}}{\partial d_{ij}} \hat{\boldsymbol{n}}_{ij}$$
 (20)

where \hat{n}_{ij} is a unit vector pointing from point i to j. The factor $w_{FF} \in$ [0, 1] acts to smoothly disable the cohesion force if the quadrature pair lies beneath the bulk liquid surface; it is computed as $w_{FF} =$ 1 – clamp $(m_{L,s}/\hat{m}_L, 0, 1)$ where $m_{L,s}$ is the liquid particle mass interpolated from the background grid (refer to Section 4.3.1 for the computation of liquid particle mass distributed on background grid), and \hat{m}_L is a small positive threshold corresponding to average particle mass just beneath the free surface, e.g., $\hat{m}_L = \sqrt{2}\pi/6$ * $\rho_L d_{\rm cell\ width}^3,$ so that clamp ($m_{L,\,s}/\hat{m}_L,0,1)$ is a mollified submersion indicator function.

Let l_{ij} be the length of the source subdomain (see Figure 16). Discretizing (2), the surface energy associated to the subdomain is given by

$$dE_{s,ij}(d_{ij}, A_{L_{ij}})$$

$$= \omega_{ij}l_{ij}\sigma \left[l_{A}(d_{ij}, A_{L_{ij}}) + \sum_{k=1,2} \cos\theta_{k}l_{Sk}(d_{ij}, A_{L_{ij}})\right], \qquad (21)$$

for the i-th point connected with neighbor point j. Since we often find a connection from one hair to another in both directions, we halve the force in such cases to avoid double-counting; this is expressed in the factor ω_{ij} which is set to 0.5 if a connection exists in the opposite direction and 1 otherwise. Thus we ensure the symmetry of forces by taking the average.

The length of the liquid-air interface is computed as

$$l_{A}(d_{ij}, A_{L_{ij}}) = R(d_{ij}, A_{L_{ij}}) \left[\pi - \sum_{k=1,2} \left(\theta_k + \alpha_k(d_{ij}, A_{L_{ij}}) \right) \right]$$
(22)

and the length of the hair-air interface is

$$l_{\rm Sk}(d_{ij}, A_{L_{ij}}) = 2r_k \left[\pi - \alpha_k(d_{ij}, A_{L_{ij}}) \right], \quad k = 1, 2.$$
 (23)

Since $R(d_{ij}, A_{L_{ij}})$ and $\alpha_k(d_{ij}, A_{L_{ij}})$ are implicitly defined by d_{ij} and $A_{L_{ij}}$, we precompute $\frac{\partial \mathrm{d} E_{s,ij}}{\partial d}$ and store its values into a table for efficiency, as described in Section S3 in the supplemental material.

4.1.2 Time Integration. We integrate the elastic rods in time using the stable constraint-based solver of Tournier et al. [2015]. This accounts for the internal forces (stretching, bending, twisting) and external forces of cohesion/repulsion, drag, and bulk pressure. (The details of bulk pressure force are presented in §4.3). During integration, the effective mass of hair above liquid is calculated as the actual mass of hair plus the mass of reduced liquid; while the effective mass of the hair underwater is just the actual mass of the hair. For stable integration, we modulate the reduced-liquid mass with w_{FF} (see *Force computation* above) to enable a smooth transition for the effective hair mass around the liquid-air interface.

Preconditioning via local solves. We accelerate our solver using a novel preconditioner. When many hairs adhere to one another, a large number of constraints are created between individual hairs, and the resulting global interactions give rise to linear systems that are difficult to solve efficiently. Furthermore, even the construction of the stiffness matrix [Tournier et al. 2015] K can have a substantial performance overhead.

Observing that the adhesive force between hairs is the only type of constraint that causes off-diagonal blocks to appear in the stiffness matrix, we developed a preconditioning strategy for the conjugate gradient method that exploits this fact.

Before solving the large globally coupled system, we first build and solve the linear system corresponding to each hair strand independently of other strands, and ignoring adhesion. Observe that the stiffness matrix can be decomposed into a sum of individual hair stiffness matrices and a cohesion stiffness matrix, such that for any vector x,

$$K\mathbf{x} = \sum_{i}^{N} K_{i} S_{i} \mathbf{x} + K_{G} \mathbf{x}, \tag{24}$$

where N is the number of hairs, and S_i is a diagonal selection matrix whose j-th term is one if the j-th degree of freedom belongs to the i-th hair and zero otherwise. This effectively pulls out the entries of \boldsymbol{x} for a single hair into a shorter vector matching the dimensions of the stiffness matrix K_i corresponding to the i-th hair. The matrix K_G encodes inter-hair coupling components. Therefore in K_i only a few degree of freedoms are involved, and these smaller systems can be solved in parallel for all the hairs.

Using the locally-solved velocity as an initial guess, we begin the preconditioned conjugate gradient method (PCG), using the local matrices for preconditioning. Each local matrix is small, banded, and remains fixed between PCG iterations; it can therefore be easily factored at the beginning of the PCG loop, and solved in parallel with a fast banded solver. To describe in detail the full algorithm for this process requires also to summarize the method and notation of Tournier et al. [2015]; for details, refer to Section S4 of our supplemental document.

We compare our PCG with other techniques (refer to Section 5 and Figure 22), namely, a conjugate gradient solver preconditioned with the inversed diagonal terms of matrix K and initialized with the locally-solved velocity (denoted as $Initialized\ DPCG$), a regular conjugate gradient solver with the last velocity as an initial guess (denoted as CG), and the sparse LDLT solver in the Eigen library [Guennebaud et al. 2010] (denoted as LDLT). We show that our method is more efficient than the others in terms of both iteration counts and timing.

4.2 Hair-Reduced Liquid Simulation

We compute the flow of liquid clinging to the hair surface using the hair-reduced liquid model developed in §3.2. By assuming that the thin liquid is always rotationally-symmetric about the hair centerline, the state is captured by two scalar fields, liquid depth h(x) and velocity u(x), as a function of hair centerline arclength parameter x.

Since the hair centerline accelerates over time, these local reduced-liquid coordinates live on a non-inertial reference frame, giving rise to inertial forces acting on the reduced-liquid system.

The inertial force at a position x of the hair appears as an additional acceleration, $-e^T(x)a(x)$, on the right hand side of (12). The force opposes the acceleration of the hair a(x) as projected onto the centerline unit tangent e(x).

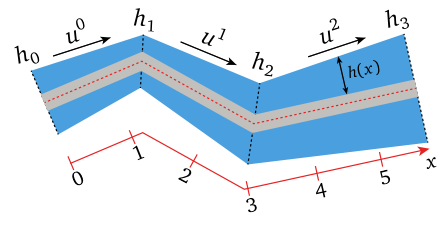


Fig. 17. Discretized Reduced-Liquid Flow Along Hair

Discretization. Consider a single hair represented by M vertices. Adopting the notation of Bergou et al. [2008], we distinguish between primal quantities, associated with vertices and decorated with lower indices, from dual quantities, associated with edges and decorated with upper indices. We discretize u(x) using a piecewise constant approximation over the centerline edges $1, \ldots, M-1$ with edge-based coefficients $\{u^1, u^2, \ldots, u^{M-1}\}$. We discretize h(x) via a piecewise linear approximation over the centerline edges with vertex-based coefficients $\{h_1, h_2, \ldots, h_M\}$ (see Fig. 17). The vertex-based length l_i for hair vertex i is computed as the averaged edge length of its neighbor edges (a.k.a. $l_i = (l^{i-1} + l^i)/2$, where l^i is the length of edge i).

Velocity update. Denoting the time step by a superscript (k), we solve the momentum equation of (12) with a semi-Lagrangian technique [Stam 1999]. We backtrace the velocity *along the centerline*, sampling the velocity upstream

$$\tilde{u}^{j,(k)} = u(x^j - u^{j,(k)} \Delta t),$$
 (25)

where x^j is the arclength parameter for the midpoint of edge j, and Δt is the time step.

We evaluate a surface-tension induced vertex-based pressure $p_i = \sigma(Lh)_i$, where L is the univariate second finite difference operator and $\sigma(Lh)_i$ accounts for the surface tension energetic preference for linearly varying height fields [Azencot et al. 2015].

The gravitational acceleration $per\ edge$ along the tangential direction of edge i as $g\cdot e_i$. The velocity is then explicitly updated as

$$u^{j,(k+1)} = \tilde{u}^{j,(k)} - \frac{\Delta t}{\rho_L} (\operatorname{grad} p)^{j,(k)} + \Delta t (\boldsymbol{g} \cdot \boldsymbol{e})$$
 (26)

where grad is the staggered grid gradient operator from vertex- to edge-based quantities.

Evolving liquid depth. Next, we solve the conservation law of mass (13). First, we compute $H_j = (h_j + r_j)^2 - r_j^2$ on each hair vertex j, where r_j is the constant hair radius at the vertex j. Then, (13) is discretized into

$$\frac{H_{j}^{(k+1)} - H_{j}^{(k)}}{\Delta t} + \langle \operatorname{grad} u \rangle_{j}^{k+1} H_{j}^{k+1} + \langle u^{i,(k+1)} (\operatorname{grad} H)^{i,(k+1)} \rangle_{j}^{i} = 0,$$
(27)

where $(\operatorname{grad} u)_j$ is the staggered grid gradient of the edge-based quantity u, producing vertex-based gradient value. $(\operatorname{grad} H)^i$ is the staggered grid gradient of vertex-based quantity H, producing edge-based gradient value. The operator $\langle \cdot \rangle_j^i$ converts edge-based quantities into vertex-based quantities. In particular, if the edge i and i+1 shares the vertex j, then an edge-based quantity v^i is converted into vertex-based quantity at the vertex j, using a weighted average with the edge lengths l^i and l^{i+1} ,

$$\langle v \rangle_j^i = \frac{1}{l_i + l_{i+1}} (v^i l^i + v^{i+1} l^{i+1}).$$

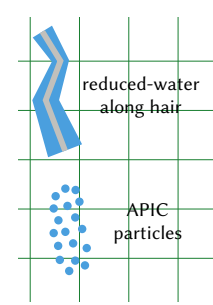
We apply absorbing boundary conditions for free hair tips so that liquid flows freely "off" (i.e., to be converted to dripping particles). For hair that stems from a solid object, we apply reflecting boundary conditions at the solid.

In our simulation, we also incorporated liquid transfer across multiple hairs into our reduced-water propagation scheme, in a simple manner (Figure 11). Specifically, we detect proximate hairs, construct a graph structure of pseudo-edges between nearby vertices, and use (only) pressure gradients to determine the flow across them, with coefficients per equation (16). However, this capillary flow phenomenon occurs at slower time-scales compared to the inertia-dominated effects we focus on. We therefore suspect that this feature has minimal effect on our main results; hence we relegate the details to Section S5 in the supplemental material.

4.3 Bulk Fluid Simulation

To simulate bulk volumes of liquid not attached to the hair itself, we adopt the affine particle-in-cell (APIC) method [Jiang et al. 2015], which offers reduced velocity dissipation and good preservation of linear and angular momentum.

At each step the fluid mass and momentum are transferred back and forth between a background grid and a set of fluid particles, allowing forces to be computed on the Eulerian grid and advection to be done in a Lagrangian fashion. This facilitates coupling between our system's components (recall Fig. 15) for both drag and pressure. APIC's pervasive use of fluid particles also conveniently enables us to treat the volume of hair-reduced liquid as a secondary *continu*-



ous set of particles that likewise exchange mass and momentum with the grid, when determining the influence of pressure.

4.3.1 Transfer: Particles to Grid. Following the APIC scheme, we first compute mass and momentum on grid faces in the x, y, and z directions; these quantities must be transferred from the nearby Lagrangian representations at each step. Following the standard APIC notation, we have

$$m_{ai}^{n} = \sum_{p} m_{p} w_{aip}^{n}$$
 and
 $m_{ai}^{n} u_{ai}^{n} = \sum_{p} m_{p} w_{aip}^{n} \left[e_{a}^{T} u_{p}^{n} + (c_{pa}^{n})^{T} (x_{ai} - x_{p}^{n}) \right],$ (28)

where the first equation accumulates mass, and the second accumulates momentum. The subscript a indicates an x-, y-, or z- direction, n is the index of the time step, p is a fluid particle index, i indexes a grid face, u_p^n is the liquid particle velocity, x is the position of a grid face centre or particle depending on the subscript, and e_a is a unit vector in the direction a. We use w_{aip}^n to denote the trilinear interpolation weight that transfers the information on particle p to grid face i for direction a, and e_{pa}^n is a vector introduced for the purpose of preserving the affine velocity field. These equations precisely follow Jiang et al. [2015].

4.3.2 Drag force. The motion of underwater hair is affected by fluid drag forces, as introduced in §3.3 and applied numerically during time integration of the hair §4.1.2, in which we define the effective mass of hair underwater as the actual mass of hair so that the drag force acts on the correct amount of mass. Otherwise, if

the reduced-liquid mass is also counted underwater during integration, the drag force will be decreased. Besides, since the bulk liquid velocity has been extrapolated for several layers into the air, we modulate the drag force applied with $1-w_{\rm FF}$ to prevent the hairs from being dragged by the air.

Naturally, Newton's third law dictates that an opposing force must be applied to the liquid, whose momentum is now stored in the grid. Our approach will be to rasterize the force that the hair exchanges with the fluid due to drag. We start with determining the reduced-liquid force per grid face. Viewing the hair strands as continuous particle sets, we compute the relevant force by integrating along the portion of each hair strand within the given cell. We index hair segments with t, the averaged drag force on a particular fluid grid face is found by summing over all segments t using

$$D_{\text{ai}}^n = \left[\sum_t \int_{l_t} w_{ai}^n(s) ds \right]^{-1} \sum_t \left[\boldsymbol{e}_a^T \int_{l_t} w_{ai}^n(s) f_{t,d}^n(s) ds \right],$$

where l_t indicates the integration path along the hair segment t inside the cell, and $w_{ai}^n(s)$ is the interpolation weight from a point s on the hair to the grid face i in direction a, and $f_{t,d}^n(s)$ is the drag force evaluated for a point s on the hair using (18). Each hair is first clipped against the relevant (staggered) cell, and the integration is approximated with two-point Gauss quadrature on each remaining segment or portion thereof.

The accumulated force is applied onto the velocity of the grid face as

$$u_{ai}^{n+1} = u_{ai}^{n} + \Delta t \frac{D_{ai}^{n}}{\rho_{L} d_{\text{coll width}}^{3}}.$$

where Δt is the time step.

4.3.3 Transfer: Reduced Liquid to Grid. Having applied the drag force to the bulk fluid, we now transfer the reduced-liquid mass and momentum onto the grid as well, before proceeding to make the full fluid volume divergence-free. We compute the necessary reduced-liquid masses per face,

$$M_{\rm ai}^n = \sum_t m_t \int_{l_t} w_{ai}^n(s) \mathrm{d}s.$$

then we simply add them to the appropriate per-face masses accumulated in (28).

With the same notation and approach, the momentum contributions from the reduced-liquid are

$$T_{\text{ai}}^{n} = \sum_{t} m_{t} \left[\boldsymbol{e}_{a}^{T} \int_{l_{t}} w_{ai}^{n}(s) \boldsymbol{u}_{t}^{n}(s) ds + \int_{l_{t}} \left(\boldsymbol{c}_{a}^{n}(s) \right)^{T} \left(\boldsymbol{x}_{ai} - \boldsymbol{x}_{t}^{n}(s) \right) ds \right],$$

$$(29)$$

where $\mathbf{c}_{a}^{n}(s)$ is a vector analogous to \mathbf{c}_{pa}^{n} in (28) for preserving the affine velocity field. The position and velocity of a point on the segment t parameterized by s are denoted by $\mathbf{x}_{t}^{n}(s)$ and $\mathbf{u}_{t}^{n}(s)$, respectively. To find $\mathbf{x}_{t}^{n}(s)$ and $\mathbf{u}_{t}^{n}(s)$ at arbitrary points along the segment we linearly interpolate from the segment's endpoints. Note that $\mathbf{u}_{t}^{n}(s)$ should be understood to be as the sum of the extrinsic (hair velocity \mathbf{v}_{H}^{n}) and intrinsic (\mathbf{u}_{L}^{n}) components of the reduced-liquid velocity, computed as $\mathbf{v}_{H}^{n} + \mathbf{u}_{L}^{n}\mathbf{e}$. We add these reduced-liquid

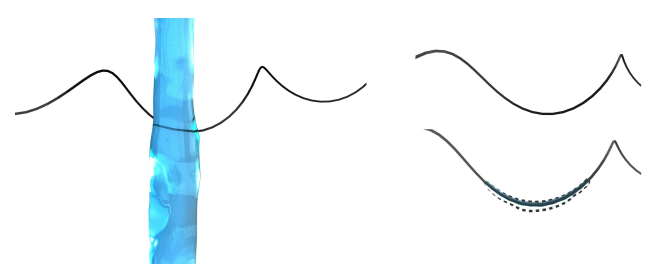


Fig. 18. Capture of liquid from a flowing stream onto the hair. Left: Water pours over a single hair. Right: A curly hair with capture turned off (above) and on (below). The captured water on the hair is highlighted by dashed lines

momentum contributions to the corresponding grid face momenta accumulated in (28).

Pressure projection. Given the grid velocities u^{n+1} after applying drag, we perform the pressure projection step of the fluid simulation which yields the divergence-free velocity field \tilde{u}^{n+1} .

4.3.4 Transfer: Grid to Particles. Next, we transfer velocities from grid faces back to particles using the standard APIC rule

$$\boldsymbol{u}_{p}^{n+1} = \sum_{a.i} w_{aip}^{n} \tilde{u}_{ai}^{n+1} \boldsymbol{e}_{a}.$$

4.3.5 Transfer: Grid to Intrinsic Reduced-Liquid Velocity. The pressure gradient from the grid should also be applied to the reduced-liquid on hairs as an impulse. We first sample the interpolated pressure gradient ∇p from the grid at the center of mass of the hair segment. We then use it to update the velocity of the reduced-liquid, considering only the component along the direction of hair segment i, using the simple update rule

$$u' = u - \frac{\Delta t}{\rho_L} \boldsymbol{e}_i^T \nabla p.$$

Transfer: Grid to hair vertices. Lastly, the pressure force should be applied to the hair itself. We apply it on the next time integration step of the hair, so we retain the pressure field for that purpose. While this implies a weak/staggered coupling, the time integration of this force is nevertheless applied implicitly in the sense that the pressure gradient in the normal direction is sampled at the unknown predicted position of hair vertices. This is done using

$$f_{\nabla p}^n = \frac{m_h}{\rho_H} \nabla p.$$

where m_h is the mass of a hair vertex including its reduced-liquid, and ρ_H is the hair density.

4.4 Reduced-Liquid Capture and Dripping

Another critical element of our model is the conservative exchange of the *volume* and associated *momentum* of liquid between the reduced and bulk fluid representations. We carry this out using new mechanisms for capture and dripping, described below. Our approach yields particles of varying sizes, since the amount of liquid entering and leaving a hair strand can be quite small; we use a particle-merging scheme similar to Ando et al. [2011] to allow such particles to coalesce into larger ones. If N_p is the target average particle number per cell, we use a default particle radius of $\sqrt{2}\Delta x/N_p$,

and we delete any particles that fall below a radius of 1×10^{-7} cm in our implementation.

In each time step we first capture liquid from nearby particles and transform it into appropriate reduced-liquid height fields on hair segments. We implement this in the following readily parallelizable fashion:

- (1) For each hair segment we find its neighboring particles within the maximal radius of attachable liquid droplets, r_{max} (see (17)), and pair the segment with each such particle. With each pair we store the arclength coordinate of the point x_C on the segment which is closest to the particle.
- (2) For each hair vertex we gather the liquid volume and momentum from the particle-segment pairs associated with its two incident hair segments. The new volume of liquid $V_{L_j}^{n+1}$ on vertex j and a net fluid velocity \boldsymbol{u}^{n+1} are computed as

$$V_{L_{j}}^{n+1} = V_{L_{j}}^{n} + \sum_{i \in \text{pairs}} V_{i}^{n+1} w(\|x_{c} - x_{j}\|),$$

$$(\rho_{L} V_{L_{j}}^{n+1} + \rho_{H} V_{H_{j}}) \boldsymbol{u}^{n+1} = \rho_{H} V_{H_{j}} \boldsymbol{v}_{H_{j}}^{n} + \rho_{L} V_{L_{j}}^{n} (\boldsymbol{v}_{H_{j}}^{n} + u_{L_{j}}^{n} \boldsymbol{e}_{H_{j}})$$

$$+ \rho_{L} \sum_{i \in \text{pairs}} V_{i}^{n+1} \boldsymbol{u}_{p}^{n+1}$$
(30)

where $w(\|x_c - x_j\|)$ is the linear interpolation kernel based on distance between the point x_c and the vertex x_j , ρ_H is the density of hair, ρ_L is the density of liquid, V_{H_j} is the volume occupied by the j-th hair vertex computed from its radius and Voronoi length, $\boldsymbol{v}_{H_j}^n$ is the hair velocity (and by association the *extrinsic* reduced-liquid velocity), $u_{L_j}^n$ is the intrinsic reduced-liquid velocity of liquid on the hair, and \boldsymbol{e}_{H_j} is the average tangent vector at hair vertex j. The corresponding amount of liquid volume transferred to the hair is deducted from the particles in the relevant particle-segment pairs.

(3) After gathering, we project the net fluid velocity \boldsymbol{u}^{n+1} onto the tangent \boldsymbol{e}_{H_j} and use it to replace the intrinsic reduced-liquid velocity; we also update the hair's total mass and the normal velocity of the hair:

$$m_{H}^{n+1} = m_{H}^{n} + \rho_{L} V_{L_{j}}^{n+1},$$

$$m_{H}^{n+1} \boldsymbol{v}_{H}^{n+1} = m_{H}^{n} \boldsymbol{v}_{H}^{n} + \rho_{L} V_{L_{j}}^{n+1} (I - \boldsymbol{e}_{H_{j}} \boldsymbol{e}_{H_{j}}^{T}) \boldsymbol{u}^{n+1}.$$
(31)

After the capture process, we allow liquid to leave the hair by carrying out a complementary dripping process as follows:

- (1) For each cell of the grid we gather the hair vertices inside it, and sum up their volume of liquid. If the hair vertex is on a hair tip, we gather the amount of liquid flowing out of the hair.
- (2) We determine if the total volume is larger than the specified threshold (§3.2) dictated by r_{max} .
- (3) We convert the volume difference between the total volume and the threshold into liquid particles of 1/4 the default particle size, and release them into the grid. We assign them (total) velocity of the liquid on the hair. Their position on

- the hair is chosen uniformly at random from within the (one-dimensional) Voronoi region of the associated vertex.
- (4) We calculate the ratio of the new volume of liquid on the hair to its past volume; for each hair vertex in the cell we rescale the height of the liquid and the corresponding mass accordingly.

With this approach, the hair easily and conservatively exchanges its associated liquid mass and momentum with the surrounding bulk flow, as seen in Figure 18.

5 RESULTS

Our results can be roughly divided into two categories: first, a set of didactic examples intended to validate individual components of our system in relative isolation, and second, a set of several more general examples of water-hair interaction demonstrating the synthesis of the complete system.

5.1 Validation Examples

Reduced-water flow. We demonstrate our hair-reduced water model by assigning an even distribution of water to a length of curly hair in Figure 13, left. Upon releasing the hair, the water flows toward the lowest point and collects, causing it to sag more than the corresponding hair without flow.

Dripping. Taking the scenario above and enabling dripping causes the collected liquid to pour off as APIC droplets in Figure 13, right. This reduces the hair effective mass so that its internal forces more easily overcome gravity and pull the hair upwards again. Performing a similar test on a vertically suspended straight hair shows that water can also pour smoothly (and conservatively) off the hair tips (Figure 9).

Inertial forces. The role of inertial forces cannot be ignored if we wish to have plausible flows along hair. Figure 8 presents a straight hair swung in a circle at a sufficient rate to cause the liquid to flow towards the tip; with inertial forces disabled the reduced-water remains stationary despite its changing reference frame.

Momentum transport. In Figure 10 we use a slanted "hair pendulum" to compare the effects of rescaling momentum vs. proper momentum transport for updating the momentum of the hair to reflect the movement of reduced-water sliding along it. Only our approach captures the expected smooth oscillation behavior without artifacts.

Liquid capture. Figure 18 shows a stream of APIC liquid falling past and around a hair; as it does so, water particles are captured and transformed into a thin layer of reduced-water on the hair surface.

Capillary transport. Figure 11 demonstrates our support for the slower capillary transport effects between contacting hairs.

Cohesion and coalescence. Our cohesion model is demonstrated in Figure 6, in which two wet hairs are placed in close proximity and pulled apart from the top. Without cohesion the hairs separate instantly; with cohesion, they remain connected until gravity and the increasing separation distance eventually breaks the connection.



Fig. 19. Wringing out water from drenched hair.

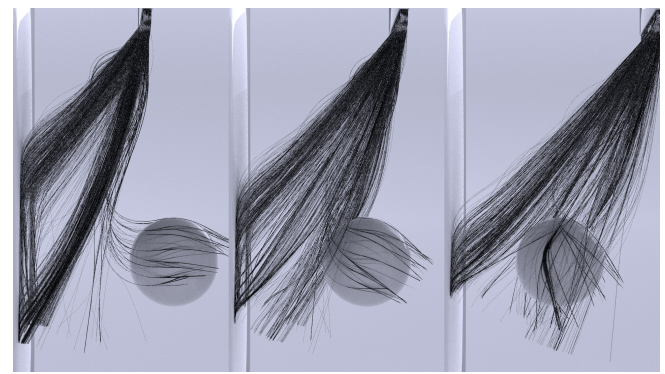


Fig. 20. Wet hairs are whipped onto a wall and then pulled off. Cohesion results between hairs and objects in the scene.

In Figure 2 we show this same cohesion effect in a more general scenario with many hairs in a row pulled out of water. The structure of coalescence in the clumping hairs provides a good qualitative match with a comparable laboratory experiment [Bico et al. 2004]. Since the cohesion force is stiff, it can be difficult to solve with a regular integrator. In Figure 22 left, we compare the convergence behavior of different iterative solvers on the linear system. We show that even for two hairs, our preconditioner (yellow curve) has a convergence rate that is several orders of magnitude faster than the other schemes we tried, namely the locally-presolved diagonallypreconditioned CG (blue curve) or the regular CG solver (green curve, mostly hidden by the blue curve).

Drag force. Pulling a single hair through a pool of water illustrates the influence of our drag force: the fluid bends the hair in opposition to its movement (Figure 14). Without drag, the hair hangs vertically, oblivious to the presence of the liquid pool.

5.2 Large-Scale Examples

Wringing out hair.. We can demonstrate several features of our method in action by pouring water onto a collection of horizontally suspended hairs to wet them, and then twisting them to effectively wring the water out (Figure 19). When the hairs are twisted, they become more closely packed. The attendant reduction in carrying capacity (17) leads to the release of bulk liquid from the hairs.

Hair whipping. Figure 20 demonstrates cohesion between hairs and solid objects with different surface curvatures, for example, a

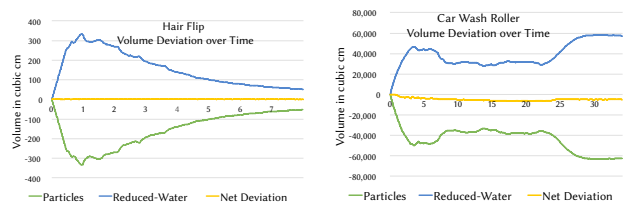


Fig. 21. Volume conservation is demonstrated by plotting the deviation of fluid volume in particles (green), reduced-water (blue), and their total (yellow). Left: Hair flip example. Right: Car wash example.

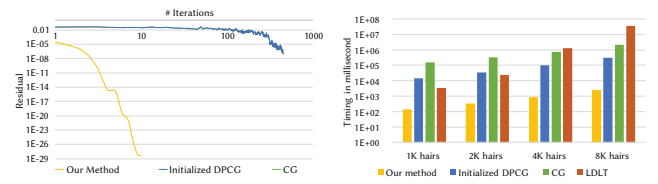


Fig. 22. Comparison between different solvers for the hair dynamics. Left: Convergence rate at 0.25 simulated seconds in *Cohesion and coalescence* (Figure 6). Right: Timing for performing one linear solve, averaged from the beginning to 0.8 simulated seconds in *Wet hair flip* (Figure 1).

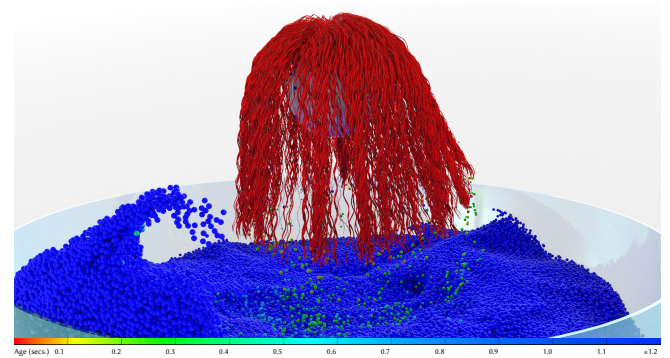


Fig. 23. Color-coded visualization of the age of fluid particles as they transition from reduced liquid flow to APIC particles.

straight wall and a ball. After the wet hair strands are pulled away from the vertical wall, some of the strands slide on the surface due to cohesion forces between the hair strands and the surface. Similarly, many strands of hair adhere to the ball throughout their relative motion.

Shaking "dog". As many pet owners can attest, dogs and other mammals often shake themselves in an alternating rotational motion to rapidly remove excess water from their bodies (and occasionally splash their owners). We simulate this process with a shaggy-haired cylindrical dog, which we pour water over and rotate rapidly side to side (Figure 25). The initial pouring causes the hair to become heavier and matted at the points of contact. Subsequent shaking helps to eject liquid off of the cylinder. Despite significant acceleration provided by our preconditioning strategy, time integration of the hair dynamics was consistently the most costly component, due to the large number of hairs and the complexity of their interactions.

Wet hair flip. Another familiar wet hair effect occurs when a head of long hair is pulled out of water and rapidly whipped forward; a substantial volume of water is carried out along with the hair and is splashed into the air (Figure 1).

In Figure 22 right, we compare among different solvers for different sizes of the scene. We show that even as the number of hairs becomes larger, our PCG solves the linear equations several orders of magnitude more efficient than other schemes. For example, when there are 8K hairs, our method (yellow bars) is two orders faster than the locally-presolved diagonally-preconditioned CG (blue bars), three orders faster than a regular CG solver (green bars), and four orders faster than Eigen's sparse LDLT solver (red bars). We only record comparisons up to 0.8 simulated seconds since performing one linear solve with LDLT in the 8K example can exceed half a day.

We also measure the total volume of reduced-hair liquid and bulk liquid over the course of the simulation. The volume of the bulk liquid is calculated as the sum of the spherical volumes of liquid associated with each APIC particle, according to each particle's radius. The volume of the hair-surface flow is calculated as the sum of the volume of the annular cylinders of liquid around the hair segments. Figure 21, left, shows that the net increase in hair-reduced water (blue curve) was offset by the net decrease in bulk liquid (green curve), yielding remarkable conservation of total liquid volume (yellow curve).

In Figure 23 we visualize the age of particles for the frame in Figure 1 to give a clearer view of how fluids drip from the hairs and change their discretization from reduced flow to particles. For a clearer view of the particles we render them with $0.7\times$ of their actual radius. The reduced flow on each hair segment is rendered as a red cylinder with the actual radius. Please refer to our supplemental video for the whole sequence.

Car wash roller. As a particularly gruelling test of our method with regards to capture and release of fluid by strands, we dunk a car wash-style roller brush into a large volume of fluid and begin spinning it at a progressively faster rate. The resulting centrifugal forces whip water out of the tips at high speed, while the spinning bristles slap back into the bulk volume and collect yet more fluid. Nonetheless, we again observe (Figure 21, right) that the net increase in reduced-water over time (blue curve) was closely offset by the net decrease in bulk liquid (green curve).

Water on mat of fur. In the Figure 3 example we pour water onto and over a sloped stationary mat of fur. The initially raised dry hair is quickly weighed down and flattened by both the flowing and captured water, clumping effects form, and reduced-water drips off the hair tips. Figure 24 demonstrates the changing clumping behavior as we increase the hair length of the simulated fur.

5.3 Performance Numbers

We collected extensive timing data to evaluate the computational cost of our method and its various components on our large-scale examples, for which a detailed breakdown is included in Figure S1 in our supplemental material. These examples employed fluid grid resolutions ranging from 64^3 to 128^3 , and hair counts ranging from 4K, for the wringing and fur examples, to 32K for the dog, and car wash scenarios. The average cost per individual time step varied between 3 and 57 seconds, while the total simulation time varied between 3.5 and 57.8 hours. The simulated time span of the examples



Fig. 24. Water is poured over four fur mats of the same hair density but of differing hair lengths, revealing increased clumping effects. Top-left: 2cm. Top-right: 3cm. Bottom-left: 4cm. Bottom-right: 5cm.

varied between 4 seconds for the water on mat of fur and 30 seconds for the car wash roller.

DISCUSSION OF LIMITATIONS AND FUTURE WORK

We have adopted or adapted a variety of physical models from prior work which are generally well-supported by experimental or analytical evidence. However, they are typically based on situations where competing factors have been isolated to focus on a single effect. In our pursuit of a very general model for animation it is possible or even likely that we have pushed these models far beyond their range of strict applicability (e.g. from single hairs to ten of thousands, or vice versa). Our calibration of the models in the full system has also been largely based on visual interpretation of the observed results, rather than carefully controlled experiments. Nevertheless, we believe our results achieve a high degree of realism.

Our capillary flow model for liquid transport between hairs is fairly naïve, since we consider only the graph structure and distance between hairs, and not an accurate structure/volume of channels between them. We found that it was much less effective when adjacent hairs are discretized in a highly non-uniform fashion. While such scenarios tend to be less common, this suggests there is room for improvement. Moreover, this effect typically occurs over longer time scales, so it may be entirely unimportant for many scenarios, including the large-scale ones we considered.

We found that the capture and dripping mechanisms can lead to a dramatic range of particles sizes spanning a few orders of magnitude, which presents a severe challenge to the reconstruction of a smooth and temporally coherent surface. This suggests two avenues. First, one could pursue improved surface reconstruction methods under such conditions, which we view as beyond the scope of the current work. Secondly, it could also be helpful to explore the development of

strategies to enforce a narrower variation in particle size. The main source of arbitrary particle sizes is our capture mechanism; while precisely conservative in terms of the water volume the hair extracts from a particle, no quantization is guaranteed on the potentially quite small particle volume left behind.

While we have sought to preserve volume throughout, our reducedwater model is not strictly conservative and leads to a small accumulating volume loss over time, particularly in the presence of large thickness gradients. Challenges of this nature remain open in computational physics as well [Bochev et al. 2013], where the transport equation may have negative solutions, and direct clamping to tends to break the divergence-free condition. Alternative options are to smooth large variations with an artificial viscosity, or to solve a least squares system for transport under a positivity constraint. In preliminary experiments in this direction, the former was only partially effective while the latter struggled to converge.

As shown in the performance table in the supplemental material, inter-hair forces dominate runtime costs, echoing the typical bottleneck in handling dry inter-hair contacts. Compared with the same elastic rod model by Kaufman et al. [2014], our linearized solver suffers less cost per time step, although it also requires smaller time steps for the stiff repulsive/cohesive constraints between hairs. Overall the cost of our hair dynamics are comparable with the dry contact timings reported in prior work that handles per-strand collisions. A model with more relaxed requirements on the time step while still correctly handling the physics between hairs requires future research.

Our current model solves degrees of freedom for all hair strands, which is slow and memory-intensive for massive numbers of hairs: for example, human heads on average have 100k hairs at the scalp, which is three times larger than the largest example presented in this paper. This approach differs from another family of methods for hair dynamics that use hierarchical structures, such as hair clusters and strips [Chai et al. 2014, 2016; Ward et al. 2007; Ward and Lin 2003; Ward et al. 2003], and can achieve interactive or even real-time performance with sophisticated collision handling. While our method focuses on the multi-scale physics of liquid-hair coupling, these prior works are targeted at level-of-detail effects for hair simulation. Combining multi-scale physics interactions for wet hairs with such reduced models for high computational performance is a potentially promising direction for future research, and we hope that our work spurs extensions to such reduced or guide-hair settings.

ACKNOWLEDGMENTS

This work was supported in part by the National Science Foundation under Grant Nos.: 14-09286, 13-19483, CAREER-1453101, and Graduate Student Research Fellowship No. DGE-16-44869, the Natural Sciences and Engineering Research Council of Canada under Grant No. RGPIN-04360-2014, the National GEM Consortium, Pixar, and Adobe. We would also like to thank Peter Yichen Chen for his assistance, Ryan Goldade for advice on surface reconstruction, Xinxin Zhang for his AMGPCG pressure solver, Fang Da and Bo Zhu for insightful discussions, Daisy Nyugen and Derrick Lim for their help on

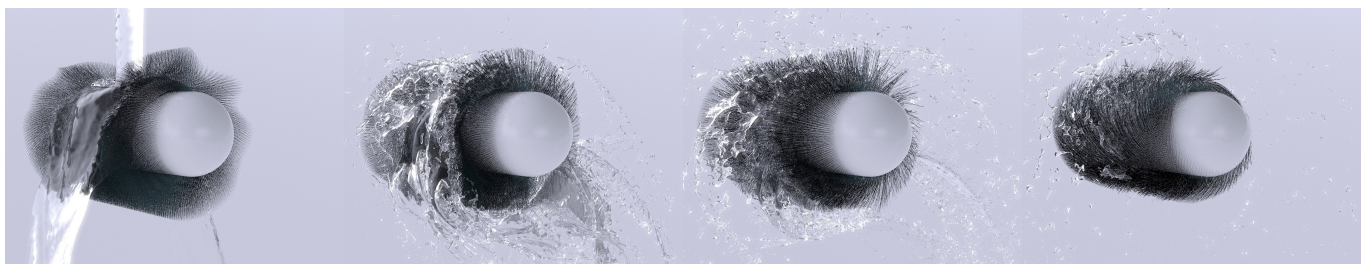


Fig. 25. A cylindrical pseudo-dog has water poured on its back; it shakes rapidly side-to-side to remove the excess water at high speed.

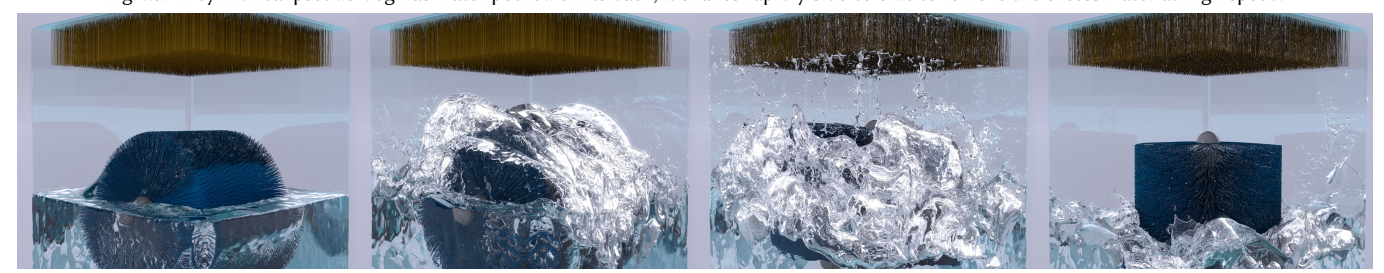


Fig. 26. A car wash roller brush spins at increasing speeds through a pool, capturing water, splashing sheets into the air, and causing the bulk volume to swirl as well.

storage and computational devices, Cristin Barghiel, Monika Janek, and Silvina Rocca for their technical support on SideFX Houdini.

REFERENCES

- Ryoichi Ando and Reiji Tsuruno. 2011. A particle-based method for preserving fluid sheets. In Proceedings of the 2011 ACM SIGGRAPH/Eurographics symposium on computer animation. ACM, 7–16.
- Omri Azencot, Orestis Vantzos, Max Wardetzky, Martin Rumpf, and Mirela Ben-Chen. 2015. Functional thin films on surfaces. In Proceedings of the 14th ACM SIGGRAPH/Eurographics Symposium on Computer Animation. ACM, 137–146.
- C Barba, M Martí, J Carilla, AM Manich, and L Coderch. 2013. Moisture sorption/desorption of protein fibres. Thermochimica acta 552 (2013), 70–76.
- Christopher Batty, Florence Bertails, and Robert Bridson. 2007. A fast variational framework for accurate solid-fluid coupling. ACM Transactions on Graphics (TOG) 26, 3 (2007), 100.
- Miklos Bergou, Basile Audoly, Etienne Vouga, Max Wardetzky, and Eitan Grinspun. 2010. Discrete viscous threads. ACM Transactions on Graphics (TOG) 29, 4 (2010), 116.
- Miklós Bergou, Max Wardetzky, Stephen Robinson, Basile Audoly, and Eitan Grinspun. 2008. Discrete elastic rods. *ACM Transactions on Graphics (TOG)* 27, 3 (2008), 63:1–63:12.
- Florence Bertails, Basile Audoly, Bernard Querleux, Frédéric Leroy, Jean-Luc Lévêque, and Marie-Paule Cani. 2005. Predicting natural hair shapes by solving the statics of flexible rods. In *Eurographics short papers*.
- José Bico, Benoit Roman, Loic Moulin, and Arezki Boudaoud. 2004. Adhesion: elastocapillary coalescence in wet hair. Nature 432, 7018 (2004), 690.
- Pavel Bochev, Denis Ridzal, and Mikhail Shashkov. 2013. Fast optimization-based conservative remap of scalar fields through aggregate mass transfer. J. Comput. Phys. 246 (2013), 37–57.
- Robert Bridson. 2015. Fluid simulation for computer graphics, 2nd edition. A. K. Peters, Ltd.
- Menglei Chai, Changxi Zheng, and Kun Zhou. 2014. A reduced model for interactive hairs. ACM Transactions on Graphics (TOG) 33, 4 (2014), 124.
- Menglei Chai, Changxi Zheng, and Kun Zhou. 2016. Adaptive Skinning for Interactive Hair-Solid Simulation. IEEE transactions on visualization and computer graphics (2016).
- R. V. Craster and O. K. Matar. 2006. On viscous beads flowing down a vertical wire. J. Fluid Mech. 553 (2006), 85–105.
- Andrew K. Dickerson, Zachary G. Mills, and David L. Hu. 2012. Wet mammals shake at tuned frequencies to dry. *Journal of the Royal Society Interface* 9, 77 (2012), 3208–3218
- J. E. Drummond and M. I. Tahir. 1984. Laminar viscous flow through regular arrays of parallel solid cylinders. *International Journal of Multiphase Flow* 10, 5 (1984), 515–540
- C. Duprat, S. Protiere, A. Y. Beebe, and H. A. Stone. 2012. Wetting of flexible fibre arrays. Nature 482, 7386 (2012), 510–513.

- Sabri Ergun. 1952. Fluid flow through packed columns. Chem. Eng. Prog. 48 (1952),
- Galen Gornowicz and Silviu Borac. 2015. Efficient and stable approach to elasticity and collisions for hair animation. In Proceedings of the 2015 Symposium on Digital Production. ACM, 41–49.
- Gaël Guennebaud, Benoît Jacob, and others. 2010. Eigen v3. http://eigen.tuxfamily.org. (2010).
- Sunil Hadap, Marie-Paule Cani, Florence Bertails, Ming Lin, Kelly Ward, Stephen Marschner, Tae-Yong Kim, and Zoran Kacic-Alesic. 2007. Strands and hair - Modeling, simulation and rendering. In SIGGRAPH Courses. 1–150.
- Sunil Hadap and Nadia Magnenat-Thalmann. 2001. Modeling dynamic hair as a continuum. Computer Graphics Forum 20, 3 (2001), 329–338.
- Dongsoo Han and Takahiro Harada. 2013. Tridiagonal matrix formulation for inextensible hair strand simulation. In *Proceedings of the Workshop on Virtual Reality Interaction and Physical Simulation*. The Eurographics Association.
- JGI Hellström and TS Lundström. 2006. Flow through porous media at moderate Reynolds number. In *International Scientific Colloquium: Modelling for Material Processing*, Vol. 2, 129–134.
- Hayley Iben, Mark Meyer, Lena Petrovic, Olivier Soares, John Anderson, and Andrew Witkin. 2013. Artistic simulation of curly hair. In Proceedings of the 12th ACM SIGGRAPH/Eurographics Symposium on Computer Animation. ACM, 63–71.
- Markus Ihmsen, Jens Orthmann, Barbara Solenthaler, Andreas Kolb, and Matthias Teschner. 2014. SPH fluids in computer graphics. In Eurographics State of the Art Reports.
- Graham W. Jackson and David F. James. 1986. The permeability of fibrous porous media. *The Canadian Journal of Chemical Engineering* 64, 3 (1986), 364–374.
- Chenfanfu Jiang, Craig Schroeder, Andrew Selle, Joseph Teran, and Alexey Stomakhin. 2015. The affine particle-in-cell method. ACM Transactions on Graphics (TOG) 34, 4 (2015), 51.
- Michael Kass and Gavin Miller. 1990. Rapid, stable fluid dynamics for computer graphics. SIGGRAPH Comput. Graph. 24, 4 (1990), 49–57.
- Danny M. Kaufman, Rasmus Tamstorf, Breannan Smith, Jean-Marie Aubry, and Eitan Grinspun. 2014. Adaptive nonlinearity for collisions in complex rod assemblies. ACM Transactions on Graphics (TOG) 33, 4, Article 123 (2014), 12 pages.
- Tassilo Kugelstadt and Elmar Schömer. 2016. Position and orientation based Cosserat rods. In Proceedings of the ACM SIGGRAPH/Eurographics Symposium on Computer Animation. Eurographics Association, 169–178.
- Toon Lenaerts, Bart Adams, and Philip Dutré. 2008. Porous flow in particle-based fluid simulations. ACM Transactions on Graphics (TOG) 27, 3 (2008), 49.
- Guoping Lian, Colin Thornton, and Michael J Adams. 1993. A theoretical study of the liquid bridge forces between two rigid spherical bodies. Journal of colloid and interface science 161, 1 (1993), 138–147.
- Wei-Chin Lin. 2014. Coupling hair with smoothed particle hydrodynamics fluids. In Proceedings of the Workshop on Virtual Reality Interaction and Physical Simulation. Wei-Chin Lin 2015. Roundary, handling and propose flow for fluidshair interactions.
- Wei-Chin Lin. 2015. Boundary handling and porous flow for fluid-hair interactions. Computers and Graphics 52 (2015), 33–43.
- T Liu, KF Choi, and Y Li. 2007. Capillary rise between cylinders. *Journal of physics D: Applied physics* 40, 16 (2007), 5006.

- Élise Lorenceau, Christophe Clanet, and David Quéré. 2004. Capturing drops with a thin fiber. Journal of colloid and interface science 279, 1 (2004), 192-197.
- Aleka McAdams, Andrew Selle, Kelly Ward, Eftychios Sifakis, and Joseph Teran. 2009. Detail preserving continuum simulation of straight hair. ACM Transactions on Graphics (TOG) 28, 3 (2009), 62.
- José Meseguer and Angel Sanz. 1985. Numerical and experimental study of the dynamics of axisymmetric liquid bridges. Journal of Fluid Mechanics 153 (1985), 83-101.
- Rajat Mittal and Gianluca Iaccarino. 2005. Immersed boundary methods. Annual review of fluid mechanics 37 (2005), 239-261.
- J. J. Monaghan. 1994. Simulating free surface flows with SPH. J. Comp. Phys. 110, 2 (1994), 399-406.
- Matthias Müller, David Charypar, and Markus Gross. 2003. Particle-based fluid simulation for interactive applications. In Symposium on Computer Animation. 154-159.
- Matthias Müller, Tae-Yong Kim, and Nuttapong Chentanez. 2012. Fast simulation of inextensible hair and fur.. In Proceedings of the Workshop on Virtual Reality Interaction and Physical Simulation, Vol. 12. 39-44.
- P Nithiarasu, KN Seetharamu, and T Sundararajan. 1997. Natural convective heat transfer in a fluid saturated variable porosity medium. International Journal of Heat and Mass Transfer 40, 16 (1997), 3955-3967.
- C. Py, R. Bastien, José Bico, B. Roman, and A. Boudaoud. 2007. 3D aggregation of wet fibers. Europhysics letters 77, 4 (2007), 44005.
- Avi Robinson-Mosher, Tamar Shinar, Jon Gretarsson, Jonathan Su, and Ronald Fedkiw. 2008. Two-way coupling of fluids to rigid and deformable solids and shells. ACM Transactions on Graphics (TOG) 27, 3 (2008), 46.
- Benoit Roman and José Bico. 2010. Elasto-capillarity: deforming an elastic structure with a liquid droplet. Journal of Physics: Condensed Matter 22, 49 (2010), 493101.
- W. Rungjiratananon, Y. Kanamori, and T. Nishita. 2012. Wetting effects in hair simulation. Computer Graphics Forum 31, 7 (2012), 1993-2002.
- A. S. Sangani and A. Acrivos. 1982. Slow flow past periodic arrays of cylinders with application to heat transfer. International Journal of Multiphase Flow 8, 3 (1982), 193-206.
- Andrew Selle, Michael Lentine, and Ronald Fedkiw. 2008. A mass spring model for hair simulation. ACM Transactions on Graphics (TOG) 27, 3 (2008), 64.
- Kiran Singh, John R. Lister, and Dominic Vella. 2014. A fluid-mechanical model of elastocapillary coalescence. J. Fluid Mech. 745 (2014), 621-646.
- Jos Stam. 1999. Stable fluids. In Proceedings of the 26th annual conference on Computer graphics and interactive techniques. ACM Press/Addison-Wesley Publishing Co., 121 - 128.
- Triantafyllos Stylianopoulos, Andrew Yeckel, Jeffrey J Derby, Xiao-Juan Luo, Mark S Shephard, Edward A Sander, and Victor H Barocas. 2008. Permeability calculations in three-dimensional isotropic and oriented fiber networks. Physics of Fluids 20, 12 (2008), 123601.
- Maxime Tournier, Matthieu Nesme, Benjamin Gilles, and François Faure. 2015. Stable constrained dynamics. ACM Transactions on Graphics (TOG) 34, 4 (2015), 132.
- Alexander Virozub, Nir Haimovich, and Simon Brandon. 2009. Three-dimensional simulations of liquid bridges between two cylinders: forces, energies, and torques. Langmuir 25, 22 (2009), 12837-12842.
- C. B. Vreugdenhil. 1994. Numerical methods for shallow-water flow. 262 pages.
- Huamin Wang, Gavin Miller, and Greg Turk. 2007. Solving general shallow wave equations on surfaces. In Proceedings of the 2007 ACM SIGGRAPH/Eurographics symposium on Computer animation. Eurographics Association, 229-238.
- Qianbin Wang, Bin Su, Huan Liu, and Lei Jiang. 2014. Chinese brushes: Controllable liquid transfer in ratchet conical hairs. Advanced Materials 26, 28 (2014), 4889-4894.
- Kelly Ward, Florence Bertails, Tae-Yong Kim, Stephen R. Marschner, Marie-Paule Cani, and Ming C. Lin. 2007. A survey on hair modeling: Styling, simulation, and rendering. IEEE TVCG 13, 2 (2007), 213-234.
- Kelly Ward, Nico Galoppo, and Ming C. Lin. 2004. Modeling hair influenced by water and styling products. In Computer Animation and Social Agents.
- Kelly Ward, Nico Galoppo, and Ming C Lin. 2007. Interactive virtual hair salon. Presence: Teleoperators and Virtual Environments 16, 3 (2007), 237-251.
- Kelly Ward and Ming C Lin. 2003. Adaptive grouping and subdivision for simulating hair dynamics. In Proceedings of 11th Pacific Conference on Computer Graphics and Applications, IEEE, 234-243.
- Kelly Ward, Ming C Lin, Lee Joohi, Susan Fisher, and Dean Macri. 2003. Modeling hair using level-of-detail representations. In Proceedings of 16th International Conference on Computer Animation and Social Agents. IEEE, 41-47.
- Edward W Washburn. 1921. The dynamics of capillary flow. Physical review 17, 3 (1921), 273,
- Stephen Whitaker. 1996. The Forchheimer equation: a theoretical development. Transport in Porous media 25, 1 (1996), 27-61.
- Thomas Young. 1805. An essay on the cohesion of fluids. Phil. Trans. R. Soc. Lond. 95 (1805), 65-87.